

Article

In Operando Probing Sodium-incorporation in NASICON Nanomaterial: Asymmetric Reaction and Electrochemical Phase Diagram

Guobin Zhang, Tengfei Xiong, Mengyu Yan, Yanan Xu, Wenhao Ren, Xu Xu, Qiulong Wei, and Liqiang Mai

Chem. Mater., **Just Accepted Manuscript** • DOI: 10.1021/acs.chemmater.7b00957 • Publication Date (Web): 13 Sep 2017Downloaded from <http://pubs.acs.org> on September 19, 2017

Just Accepted

“Just Accepted” manuscripts have been peer-reviewed and accepted for publication. They are posted online prior to technical editing, formatting for publication and author proofing. The American Chemical Society provides “Just Accepted” as a free service to the research community to expedite the dissemination of scientific material as soon as possible after acceptance. “Just Accepted” manuscripts appear in full in PDF format accompanied by an HTML abstract. “Just Accepted” manuscripts have been fully peer reviewed, but should not be considered the official version of record. They are accessible to all readers and citable by the Digital Object Identifier (DOI®). “Just Accepted” is an optional service offered to authors. Therefore, the “Just Accepted” Web site may not include all articles that will be published in the journal. After a manuscript is technically edited and formatted, it will be removed from the “Just Accepted” Web site and published as an ASAP article. Note that technical editing may introduce minor changes to the manuscript text and/or graphics which could affect content, and all legal disclaimers and ethical guidelines that apply to the journal pertain. ACS cannot be held responsible for errors or consequences arising from the use of information contained in these “Just Accepted” manuscripts.

1
2
3
4 ***In Operando* Probing Sodium-incorporation in NASICON**
5
6 **Nanomaterial: Asymmetric Reaction and Electrochemical Phase**
7
8 **Diagram**
9

10
11 Guobin Zhang^{†, §}, Tengfei Xiong^{†, §}, Mengyu Yan^{†, ‡, *}, Yanan Xu[†], Wenhao Ren[†], Xu
12 Xu[†], Qiulong Wei[†], Liqiang Mai^{†, //, *}
13
14

15
16 † State Key Laboratory of Advanced Technology for Materials Synthesis and
17 Processing, International School of Materials Science and Engineering, Wuhan
18 University of Technology, Wuhan 430070, P. R. China
19
20

21
22 ‡ Materials Science and Engineering Department, University of Washington, Seattle,
23 Washington, 98195-2120, USA
24

25
26 // Department of Chemistry, University of California, Berkeley, California 94720,
27 United States
28
29
30
31
32
33
34
35
36
37
38
39
40
41
42
43
44
45
46
47
48
49
50
51
52
53
54
55
56
57
58
59
60

1
2
3
4
5
6
7
8
9
10
11
12
13
14
15
16
17
18
19
20
21
22
23
24
25
26
27
28
29
30
31
32
33
34
35
36
37
38
39
40
41
42
43
44
45
46
47
48
49
50
51
52
53
54
55
56
57
58
59
60

ABSTRACT: NASICON-type materials are one of the most promising cathodes for sodium-ion batteries (SIBs) due to their stable structure and the three-dimensional framework for the migration of Na^+ . During its usage, battery should hold the ability to endure sudden changes in temperature and current density, which have profound impact on battery life. However, few researches focused on the reaction mechanism under above situations. Here, the phase transformation processes of NASICON-type material, $\text{Na}_3\text{V}_2(\text{PO}_4)_3$, are investigated by applying high-resolution *in-situ* X-ray diffraction, Raman coupled with electrochemical tests under different temperatures (273 and 293 K) and scan rates (0.5, 2, 5 mV s^{-1}). The results demonstrate that the phase evolution process is one-phase solid solution during desodiation process rather than the traditionally two-phase reaction with high scan rate or low temperature. An electrochemical phase diagram is also drawn based on the in situ results, which can be used to explain the asymmetric result. This work can help understanding the phase evolution process of NASICON-type cathodes, as well as guiding the application of SIBs in various working conditions.

1. INTRODUCTION

Due to abundant resources, low cost and competitive energy densities, sodium-ion batteries (SIBs) have attracted much attention in sustainable development as well as large-scale applications to realize the utilization of reducing peak and filling valley in power grid.^{1,2} Fast Na⁺ superionic conductor (NASICON)-related compounds, as one of the typical sodium cathode materials, are of great interest due to their three-dimensional sodium transfer pathway.^{3,4} These NASICON-type materials were first studied as the solid electrolyte by few researchers such as Goodenough, Hong and Delmas.^{5, 6, 7} Then, they have been reinvestigated for their stable structure and sodium de-insertion.⁸

The NASICON-type materials are typically constructed by the isolated octahedral and tetrahedral units, which often lead to the low intrinsic electronic conductivity.^{9, 10} Maya et al. overcame the drawback by using optimizing strategies such as nanosizing and carbon coating.^{11, 12} There are also some literatures reporting the electrochemical reaction mechanism of NASICON-type materials at relatively low current density. Lim et al. used *ex situ* X-ray diffraction (XRD) to investigate the reaction mechanism at 0.2 C and found the two-phase reaction mechanism, which was further proved by Jian et al. with the employment of *in-situ* XRD at 0.1 C.^{13, 14} However, the utilization of NASICON-type materials is faced with various operating environments, including different charge/discharge rates and temperatures, which have not been fully studied. More importantly, the reaction mechanisms of NASICON-type materials and the corresponding dynamic behavior at different rates, which hidden in the

1
2
3 electrochemical process, haven't ever been explored at different reaction
4
5 temperatures.
6
7

8
9 Here, $\text{Na}_3\text{V}_2(\text{PO}_4)_3$ is selected to systematically study the reaction mechanism of
10
11 NASICON-type materials under different reaction conditions (scan rates of 0.5, 2 and
12
13 5 mV s^{-1} , temperatures of 273 and 293 K) by applying *in-situ* XRD, Raman and
14
15 electrochemical tests. The phase evolution process turns out to be an asymmetric
16
17 transformation process, where a one-phase solid solution reaction occurs during the
18
19 anodic process and a two-phase evolution is observed during cathodic period. The
20
21 electrochemical phase diagram is drawn based on the *operando* results (3C and 5C at
22
23 273, 293 and 313 K, where 1 C refers to 117 mA g^{-1} for $\text{Na}_3\text{V}_2(\text{PO}_4)_3$). With the help
24
25 of the electrochemical phase diagram, it is possible to understand the phase evolution
26
27 process of NASICON-type material to promote the development of SIBs. This work
28
29 can help understanding the functioning of this polyanionic electrode material in real
30
31 operating conditions.
32
33
34
35
36
37
38

39 40 **2. EXPERIMENTAL SECTION**

41 42 **2.1 Materials synthesis**

43
44 The $\text{Na}_3\text{V}_2(\text{PO}_4)_3/\text{C}$ particles were synthesized according to the literature¹⁵. The main
45
46 reagents NaH_2PO_4 , $\text{H}_2\text{C}_2\text{O}_4 \cdot 2\text{H}_2\text{O}$ and V_2O_5 were analytical grade, purchased from
47
48 Sinopharm Chemical Reagent Co., Ltd. (Shanghai, China). Firstly, V_2O_5 (1 mmol)
49
50 and $\text{H}_2\text{C}_2\text{O}_4 \cdot 2\text{H}_2\text{O}$ (3 mmol) were dissolved in H_2O (15 mL) and the system was
51
52 stirred for 30 min at $70 \text{ }^\circ\text{C}$. Then, NaH_2PO_4 (3 mmol) and glucose (1 mmol) were
53
54 added to the above solution with vigorously stirring for 10 min. Afterwards, dimethyl
55
56
57
58
59
60

1
2
3
4 formamide (50 mL) was added drop by drop, followed by stirring for 10 min. Next,
5
6 the solution was dried at 70 °C for 24 h to obtain the precursor. Finally, the
7
8 $\text{Na}_3\text{V}_2(\text{PO}_4)_3/\text{C}$ particles were obtained after the preheating process at 400 °C for 4 h
9
10 and the annealing process at 750 °C for 8 h in Ar, with a heating rate of 5 °C min^{-1} .
11
12

13 14 **2.2 Materials characterization**

15
16 The images of morphology and microstructure were collected by a JEOL-7100F
17
18 microscope and a JSM-2010 microscope, respectively. Element mapping was obtained
19
20 *via* an EDX-GENESIS 60S spectrometer. XRD characterization of the powder sample
21
22 and *in-situ* XRD tests of the cathode sheet were carried out with a Bruker D8
23
24 Discover X-ray diffractometer, using Cu-K α radiation ($\lambda = 1.5418 \text{ \AA}$). XRD
25
26 refinement was conducted with the software TOPAS. Figure S1 (Supporting
27
28 Information)¹⁶ shows the schematic of the *in-situ* cell. TG-DSC curves were obtained
29
30 using a Netzsch STA 449C thermal analyzer with a heating rate of 10 K min^{-1} in air.
31
32 BET(Brunauer-Emmet-Teller) surface area was calculated from nitrogen adsorption
33
34 isotherms at 77 K by using Tristar II 3020 instrument. Raman spectra were obtained
35
36 *via* a Renishaw INVIA micro-Raman spectroscopy system.
37
38
39
40
41
42
43
44

45 **2.3 Electrochemical measurements**

46
47 The 2016 coin cells were assembled in a glovebox filled with pure argon. When
48
49 sodium foil was used as the anode, the electrolyte was composed of 1 molar NaClO_4
50
51 in ethylene carbonate/dimethyl carbonate (1:1 w/w) with 5 wt% fluoroethylene
52
53 carbonate (FEC) additive. The glass fiber was used as the separator. The cathode was
54
55 obtained with 70% active material, 20% acetylene black and 10% poly
56
57
58
59
60

1
2
3 (tetrafluoroethylene) (PTFE) binder. The assembly of *in-situ* cells was similar, except
4
5
6 that Be window was used. Galvanostatic charge/discharge cycling was studied from
7
8
9 2.3-4.2 V vs. Na⁺/Na using a multi-channel battery testing system (LAND CT2001A).
10
11 The *in-situ* XRD signals were collected using the VANTEC-500 detector in a still
12
13 mode during the discharge–charge process, and each pattern took 30 s to acquire. CV
14
15 (cyclic voltammetry) and EIS (electrochemical impedance spectroscopy) were
16
17
18 obtained with an electrochemical workstation (Autolab PGSTAT302N).
19
20
21
22
23
24
25
26
27
28
29
30
31
32
33
34
35
36
37
38
39
40
41
42
43
44
45
46
47
48
49
50
51
52
53
54
55
56
57
58
59
60

3. RESULTS AND DISCUSSION

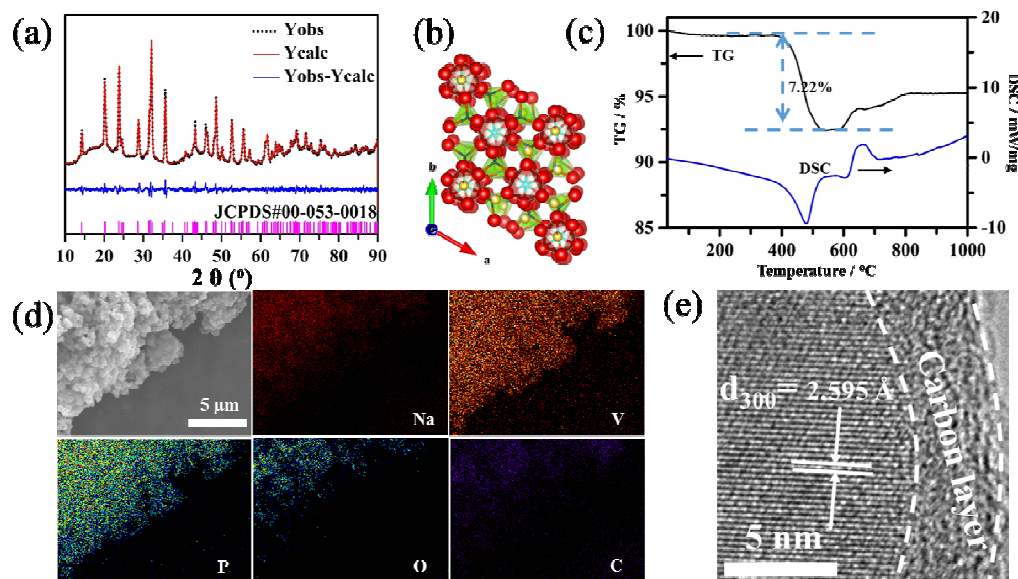


Figure 1. Characterizations of the as-synthesized material. a) XRD pattern and Rietveld refinement of Na₃V₂(PO₄)₃/C. b) Crystal structure of hexagonal Na₃V₂(PO₄)₃ along the *c* axis (yellow: Na; cyan: V; dark blue: P; red: O). c) TG-DSC curve of Na₃V₂(PO₄)₃/C with the temperature of room temperature to 1000 °C. d) Elemental mapping images of the Na₃V₂(PO₄)₃/C particles and e) HRTEM image.

The Powder XRD and further Rietveld refinement implemented by TOPAS 4.2 (a relatively low Rwp value of 3.11 is achieved) are employed to investigate the crystal structure of Na₃V₂(PO₄)₃ (Figure 1a). Rietveld result shows that the as-synthesized material is hexagonal with a space group of R-3c (lattice parameter of $a = b = 8.748$ Å, $c = 21.852$ Å, $\alpha = \beta = 90^\circ$, $\gamma = 120^\circ$) and a crystal size of 80.3 nm. The P-O tetrahedral and the V-O octahedral form the structure shown in Figure 1b.

1
2
3
4 Thermogravimetry analysis (TGA) is applied and TG curve (Figure 1c) proves that
5
6 the content of carbon is $\sim 7.22\%$. The scanning electron microscopy (SEM) (Figure
7
8 1d) shows the as-synthesized material consists of small nanosized particles. These
9
10 elements are evenly distributed as shown in the energy dispersive X-ray spectroscopic
11
12 (EDS) (Figure 1d) mapping of the material. To further investigate the carbon-coating
13
14 of the as-synthesized material, high resolution transmission electron microscopy
15
16 (HRTEM) is employed (Figure 1e) and the HRTEM image clearly shows that the
17
18 thickness of carbon shell is ~ 5 nm. The HRTEM image and the XRD fitting result
19
20 prove the preferred orientation of $\text{Na}_3\text{V}_2(\text{PO}_4)_3$ nanomaterial is (300) lattice plane
21
22 with a space distance of 2.59 \AA . BET (Brunauer–Emmet–Teller) result (Figure S2,
23
24 Supporting Information) shows that the specific surface area of the powder is 76.9 m^2
25
26 g^{-1} . The as-synthesized material delivers a capacity of 80 mA h g^{-1} after 1000 cycles at
27
28 5 C (Figure S3, Supporting Information).
29
30
31
32
33
34
35
36
37
38
39
40
41
42
43
44
45
46
47
48
49
50
51
52
53
54
55
56
57
58
59
60

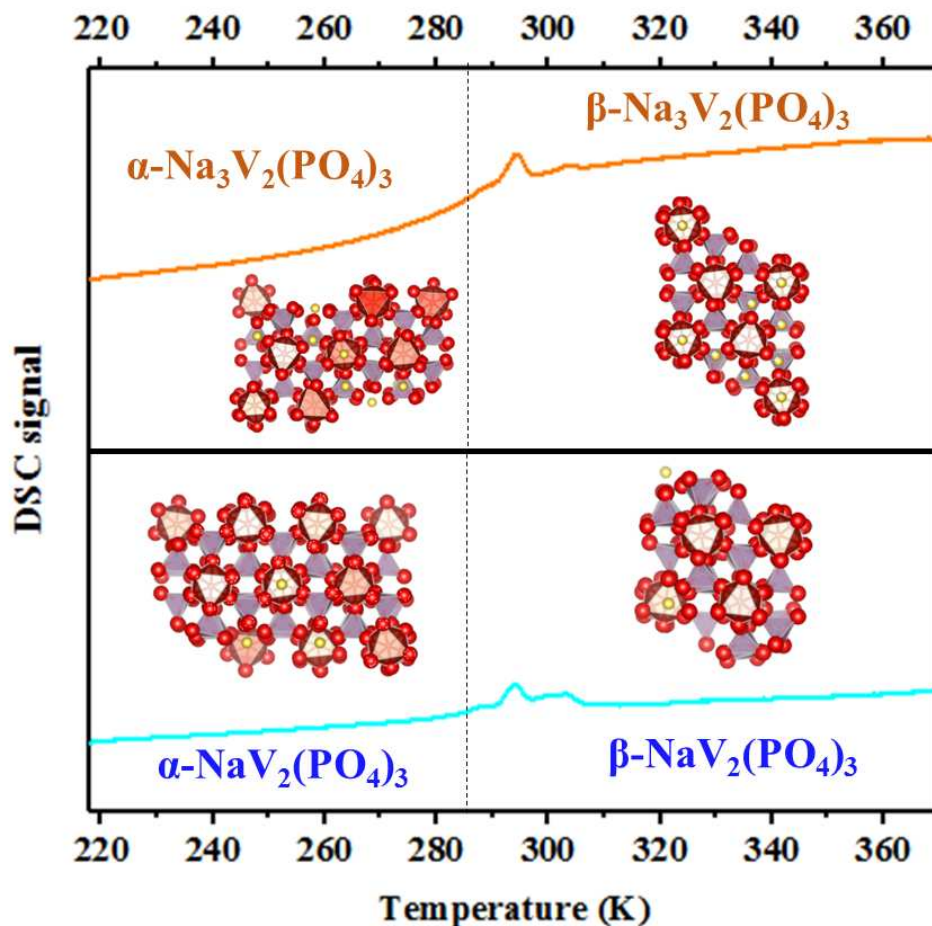


Figure 2. DSC measurement of $\text{Na}_3\text{V}_2(\text{PO}_4)_3$ and $\text{NaV}_2(\text{PO}_4)_3$ (four different crystal structures b) from 213 – 373 K (10 K min^{-1}).

To study the phase transition mechanism at different temperatures, DSC measurement was done for $\text{Na}_3\text{V}_2(\text{PO}_4)_3$ and $\text{NaV}_2(\text{PO}_4)_3$ in the temperature range of 213 – 373 K at the heating rate of 10 K min^{-1} shown in Figure 2.¹⁷ $\text{Na}_3\text{V}_2(\text{PO}_4)_3$ undergoes a distinct phase transition from α - $\text{Na}_3\text{V}_2(\text{PO}_4)_3$ to β - $\text{Na}_3\text{V}_2(\text{PO}_4)_3$ and $\text{NaV}_2(\text{PO}_4)_3$ undergoes a distinct phase transition from α - $\text{NaV}_2(\text{PO}_4)_3$ to β - $\text{NaV}_2(\text{PO}_4)_3$. As reported, phase transition from α - $\text{Na}_3\text{V}_2(\text{PO}_4)_3$ to β - $\text{Na}_3\text{V}_2(\text{PO}_4)_3$ happens at around 283 K, thus *in-situ* XRD of $\text{Na}_3\text{V}_2(\text{PO}_4)_3$ and $\text{NaV}_2(\text{PO}_4)_3$ at

1
2
3
4 temperatures of 273, 283 and 293 K in the *in-situ* cell was collected for 5 min per
5
6 pattern (Figure S4, Supporting Information). The results show that the phase
7
8 transitions of $\text{Na}_3\text{V}_2(\text{PO}_4)_3$ and $\text{NaV}_2(\text{PO}_4)_3$ happen at around 283 K. To further
9
10 determine the crystal structure of these four phases, XRD patterns of the two phases at
11
12 273 and 293 K were done for 6 hours per pattern (Figure S5, Supporting Information).
13
14 With declining the temperature, peak at $\sim 32^\circ$ shifts to the higher diffraction angle,
15
16 which indicates the shrinkage of the crystal. From the selected range of the XRD
17
18 patterns in Figure S5, the peak splitting phenomenon is apparent at 273 K for both
19
20 $\text{Na}_3\text{V}_2(\text{PO}_4)_3$ and $\text{NaV}_2(\text{PO}_4)_3$, which shows same character with the literature.¹⁷
21
22
23
24
25
26 Further XRD refinement is done to get the crystal information (Figure S6, Supporting
27
28 Information). The refinement results show that the high-site symmetry phase with
29
30 space group of $R\bar{3}c$ turns to a low-site symmetry phase of $C2/c$ at ~ 283 K for
31
32 $\text{Na}_3\text{V}_2(\text{PO}_4)_3$ and $\text{NaV}_2(\text{PO}_4)_3$.
33
34
35
36
37
38
39
40
41
42
43
44
45
46
47
48
49
50
51
52
53
54
55
56
57
58
59
60

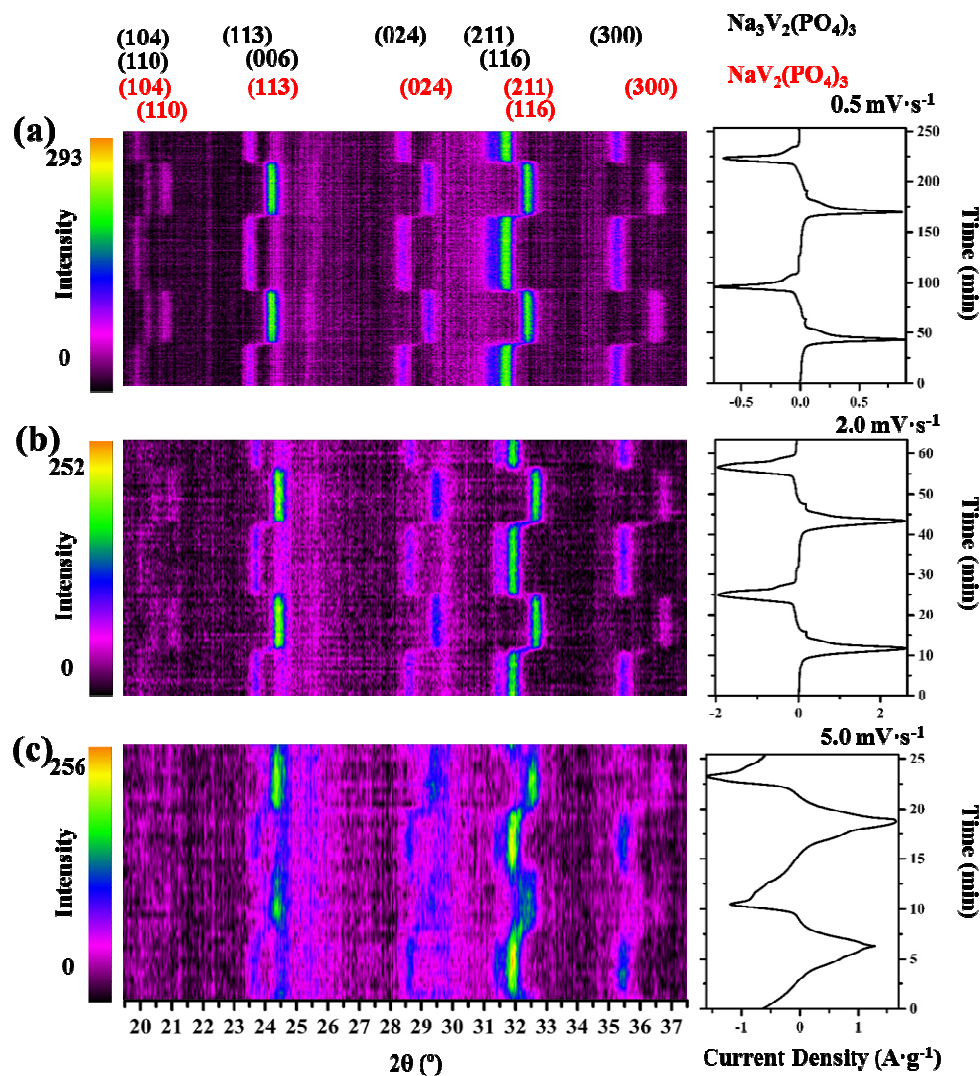


Figure 3. Two-dimensional *in-situ* XRD patterns of $\beta\text{-Na}_3\text{V}_2(\text{PO}_4)_3/\text{C}$ during the CV processes in the voltage range of 2.3 – 4.2 V at 293 K. Four peak regions (with lattice planes marked above the patterns) can be observed with the 2θ range of $19.5\text{-}37.5^\circ$. The diffraction intensity is coded with different colors shown in the scale bar on the left. Time-current density plots are shown on the right. Corresponding scan rates are a) 0.5, b) 2.0 and c) $5.0 \text{ mV}\cdot\text{s}^{-1}$ respectively.

1
2
3
4
5
6
7 *In-situ* XRD was performed at different scan rates of 0.5, 2, and 5 mV s⁻¹ (Figure
8
9 3a, b and c) under an ambient condition (293 K) to investigate the phase
10 transformation process. At a low scan rate of 0.5 mV s⁻¹ (Figure 3a), all diffraction
11 peaks can be indexed to Na₃V₂(PO₄)₃ and NaV₂(PO₄)₃ with two theta angle ranging
12 from 19.5° to 37.5°. This experiment results are in consistence with former work and
13 traditional understanding: the diffraction peaks of Na₃V₂(PO₄)₃ disappear while the
14 peaks of NaV₂(PO₄)₃ appear suddenly.¹⁴ As the scan rate increases to 2 mV s⁻¹ (Figure
15 3b), continuous positive intensities appear in the selected angle ranges, suggesting that
16 observable phases appears during the anodic period and negligibly during the cathodic
17 process. When the scan rate increases to 5 mV s⁻¹ (Figure 3c), continuous strong
18 positive intensities move to the peaks indexed to NaV₂(PO₄)₃ during the anodic
19 period. And during the cathodic process, the strong positive intensities move to the
20 diffraction peaks of Na₃V₂(PO₄)₃ with negligible breaks. This asymmetric result
21 indicates that the phase evolution process becomes different compared with the result
22 at 0.5 mV s⁻¹, where the phase transformation in the anodic progress turns out to be a
23 solid solution reaction with the increscent of scan rate. This result indicates the
24 transformation mechanism changes from the traditional two-phase transformation to a
25 one-phase solid solution reaction.
26
27
28
29
30
31
32
33
34
35
36
37
38
39
40
41
42
43
44
45
46
47
48
49
50
51
52
53
54
55
56
57
58
59
60

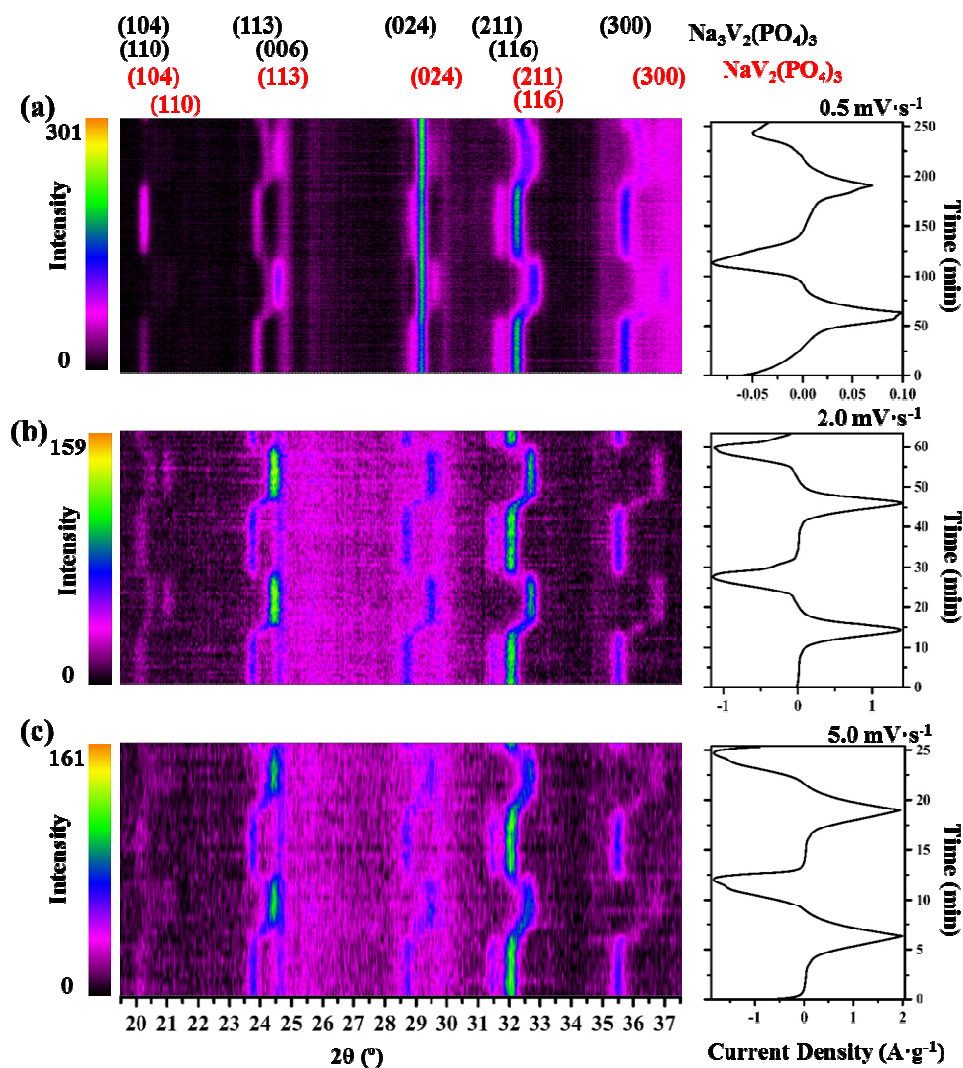
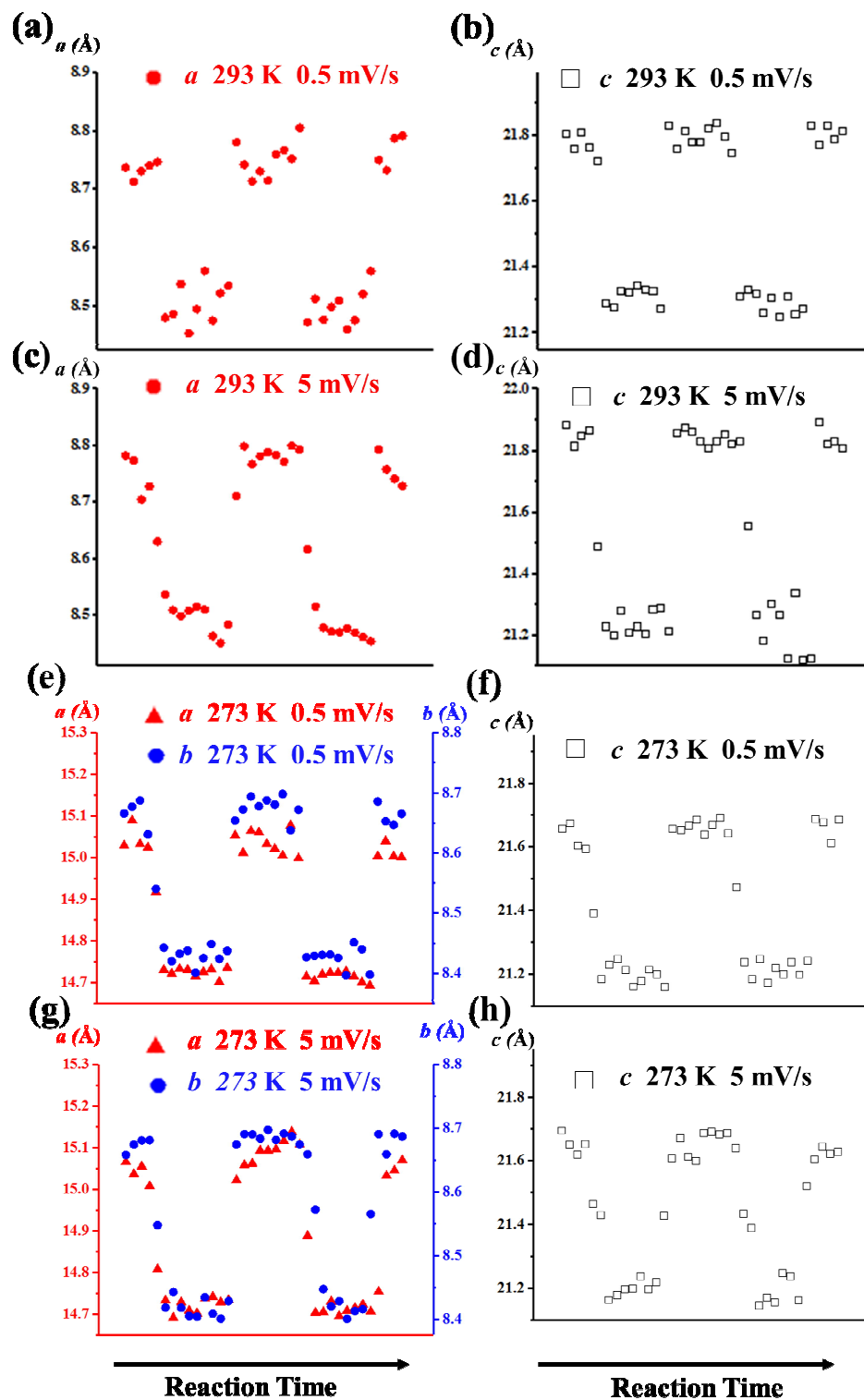


Figure 4. Two-dimensional *in-situ* XRD patterns of α - $\text{Na}_3\text{V}_2(\text{PO}_4)_3$ during the CV processes with the voltage range of 2.3 – 4.2 V at 273 K. Four peak regions (with lattice planes marked above the patterns) can be observed with the 2θ range of 19.5–37.5°. The diffraction intensity is coded with different colors shown in the scale bar on the left. Corresponding scan rates are a) 0.5, b) 2.0 and c) 5.0 $\text{mV}\cdot\text{s}^{-1}$ respectively. The neglected peaks between the two stable phases become more distinct at 273 K.

1
2
3
4
5
6
7 There is little research on the mechanism study of $\alpha\text{-Na}_3\text{V}_2(\text{PO}_4)_3$ during low
8
9 temperature. To study the low temperature reaction mechanism, *in-situ* XRD
10
11 measurements with the CV scan rates of 0.5, 2.0, and 5.0 mV s^{-1} (Figure 3a-c,
12
13 respectively) are performed at 273 K. It is found that the asymmetric reaction
14
15 becomes more obvious. Positive intensities of the diffraction peaks of $\alpha\text{-Na}_3\text{V}_2(\text{PO}_4)_3$
16
17 gradually move to the peaks of $\alpha\text{-NaV}_2(\text{PO}_4)_3$ during the anodic reaction, and jump
18
19 with negligible intensities to $\text{Na}_3\text{V}_2(\text{PO}_4)_3$ during the cathodic process at the scan rates
20
21 of 0.5 and 2 mV s^{-1} . At a high scan rate of 5.0 mV s^{-1} , the process from $\alpha\text{-NaV}_2(\text{PO}_4)_3$
22
23 to $\alpha\text{-Na}_3\text{V}_2(\text{PO}_4)_3$ becomes different where more positive intensities can be observed.
24
25 From the XRD data, it can be noted that during the anodic process the formation of
26
27 the sodium-deficient phase happens through a sort solid solution region. At the same
28
29 time, the continuous intensity distributions in the XRD patterns confirmed the
30
31 continuously lattice parameter changes, which indicate a continuous distribution of
32
33 phases with different cell parameters appearing during this process at high current
34
35 density. This kind of phase transformation not only turns the phase transformation to a
36
37 one-phase solid solution reaction process, but also buffers and enlarges the sodium ion
38
39 diffusion pathway.
40
41
42
43
44
45
46
47
48
49
50
51
52
53
54
55
56
57
58
59
60

S

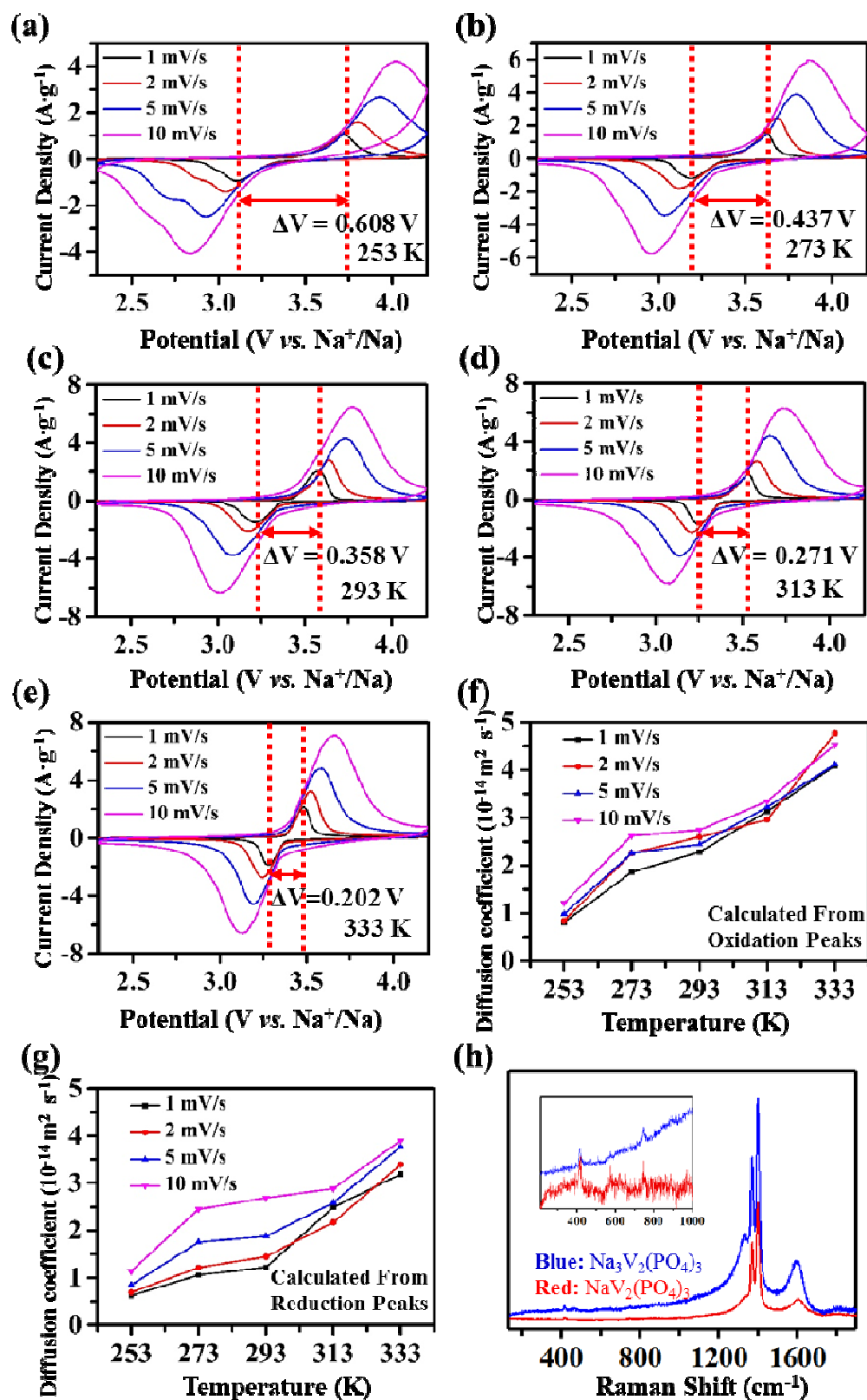


1
2
3
4 **Figure 5.** Average lattice parameter changes of a , b and c (a , b , e , f at 293 K and c , d ,
5
6 g , h at 273 K) during the CV processes calculated from *in-situ* XRD patterns in Figure
7
8 3 and Figure 4. As the temperature decreases to 273 K (Figure 4f and 4h), the lattice
9
10 parameter changes as well as the asymmetric phenomenon.
11
12

13
14
15
16
17
18 Pawley XRD refinement solution was employed to explore the lattice parameter
19
20 changes (Figure 5a-h) resulting from different temperatures (273 K and 293 K) and
21
22 different scan rates (0.5 and 5 mV s⁻¹).^{18, 19} At the scan rate of 0.5 mV s⁻¹ (Figure
23
24 4a-d), β -Na₃V₂(PO₄)₃ with lattice parameters of about $a = b = 8.748$ Å, $c = 21.852$ Å
25
26 abruptly transforms to sodium-deficient phase with lattice parameters of about $a = b =$
27
28 8.507 Å and $c = 21.713$ Å, which indicates the two-phase transition mechanism. Then
29
30 the sodium-deficient phase changes back to the original one with the instantaneous
31
32 increase of lattice parameters during the discharge process (Figure 5a and 5c).
33
34 However, at 5 mV s⁻¹, lattice parameters of the pristine gradually shift with a gentle
35
36 slope to the sodium-deficient phase during both the anodic and cathodic
37
38 electrochemical processes at 293 K (Figure 5e and 5g). This result indicates the
39
40 transformation mechanism changes from the traditional two-phase transformation to
41
42 one-phase solid solution reaction. At 273 K and 0.5 mV s⁻¹, α -Na₃V₂(PO₄)₃ with
43
44 lattice parameters of about $a = 15.037$ Å, $b = 8.662$ Å, $c = 21.660$ Å and $\beta = 90.169^\circ$
45
46 abruptly transforms to sodium-deficient phase with lattice parameters of about $a =$
47
48 14.757 Å, $b = 8.472$ Å, $c = 21.212$ Å and $\beta = 90.248^\circ$. As the temperature declines to 273
49
50 K (Figure 5f and 5h), lattice parameter changes as well as the asymmetric
51
52
53
54
55
56
57
58
59
60

1
2
3
4 phenomenon, which are pointed out in the dotted rectangle, become more obvious.

5
6 The assumption reason of the asymmetric reaction may be the different sodium-ion
7
8 diffusion coefficients. The superstructure of $\alpha\text{-Na}_3\text{V}_2(\text{PO}_4)_3$ may accelerate the
9
10 sodium transportation in the superlattice structure due to the stability of the structure.
11
12
13
14
15
16
17
18
19
20
21
22
23
24
25
26
27
28
29
30
31
32
33
34
35
36
37
38
39
40
41
42
43
44
45
46
47
48
49
50
51
52
53
54
55
56
57
58
59
60



1
2
3
4 **Figure 6.** The CV curves of $\text{Na}_3\text{V}_2(\text{PO}_4)_3$ at temperatures [a)253 K, b) 273 K, c) 293
5
6 K, d) 313 K and e) 333 K] and scan rates (1, 2, 5 and 10 mV /s), respectively. The
7
8 diffusion coefficient calculated from f) oxidation peaks and g) reduction peaks of
9
10 $\text{Na}_3\text{V}_2(\text{PO}_4)_3$ at different scan rates and different temperatures; h) the Raman shifts of
11
12 $\text{Na}_3\text{V}_2(\text{PO}_4)_3$ and $\text{NaV}_2(\text{PO}_4)_3$. (The inset plot is the selected region of 100 – 1000
13
14 cm^{-1}).

15
16
17
18
19
20
21
22
23 To further understand the phenomenon above, sodium ion diffusion coefficients in
24
25 the electrochemical processes at different temperatures (253, 273, 293, 313 and 333
26
27 K) are deduced through CV curves at different scan rates (1, 2, 5 and 10 mV s^{-1}),
28
29 which might be helpful to understand the mechanism quantitatively (Figure 6 a-e).
30
31 The voltage difference between the oxidation peak and reduction peak increases from
32
33 0.202 V to 0.608 V with the decrease of the temperature from 333 K to 253 K at 1 mV
34
35 s^{-1} . The sodium ion diffusion coefficients are determined according to the
36
37 Randles-Sevchik equation for the semi-infinite diffusion of Na^+ into or out of the
38
39 chemical host^{20,21}. The calculated diffusion coefficients from oxidation and reduction
40
41 peaks decrease by reducing temperature (Figure 6 f-g). But the decreasing trend of the
42
43 diffusion coefficient has a gently dipping at 293 K, which indicates that there may
44
45 exist different reaction mechanisms or different reaction pathways during the
46
47 electrochemical process around 293 K. Raman shifts of charged as well as discharged
48
49 state of $\text{Na}_3\text{V}_2(\text{PO}_4)_3$ are presented in Figure 6h to study the chemical bond variation
50
51 within a Raman shift range of 200 - 3000 cm^{-1} . A detailed image with a range of 200 –
52
53
54
55
56
57
58
59
60

1
2
3
4 1000 cm^{-1} in the inset plot of Figure 6h indicates that there is no peak shift. Two
5
6 intense bands at ~ 750 and 550 cm^{-1} and one strong band at $\sim 420 \text{ cm}^{-1}$ can be indexed
7
8 to the vibrations and bending modes of $[\text{VO}_6]$ octahedron and $[\text{PO}_4]$ tetrahedral.²²
9
10 Furthermore, carbon materials can be obviously observed by two characteristic bands:
11
12 D-band around 1360 cm^{-1} and G-band around 1600 cm^{-1} , which is mixed with the
13
14 band of corundum around 1367 and 1399 cm^{-1} . *In-situ* Raman measurement is
15
16 employed to characterize the reaction pathway within the Raman shift range from 200
17
18 to 1000 cm^{-1} at a current density of 1 C (Figure S7, Supporting Information). The
19
20 asymmetric reaction pathway still exists in the *in-situ* Raman results. From the
21
22 one-dimensional image (Figure S7a), the band around 420 cm^{-1} presents no changes,
23
24 while the bands around 750 and 550 cm^{-1} become weaker and weaker. All the peaks
25
26 can recover to its original state as the material returns to its discharged state. Two
27
28 dimensional image of the *in-situ* Raman spectrum (Figure S7b) shows that the
29
30 intensity changes little during the charge process but changes greatly during the
31
32 discharge process within the band range from 550 to 750 cm^{-1} . Meanwhile, strong
33
34 positive intensities appear within the same range during the discharge process
35
36 highlighted by the dash line. In conclusion, the cathodic process can be transformed
37
38 more quickly compared with the anodic process due to the solid state reaction, which
39
40 is captured in the *in-situ* XRD and *in-situ* Raman results. The asymmetric reaction
41
42 pathway observed in our work can accelerate the sodium ion diffusion and thus
43
44 mitigate the decrement of the sodium ion diffusion coefficient with the decline of
45
46 temperature.
47
48
49
50
51
52
53
54
55
56
57
58
59
60

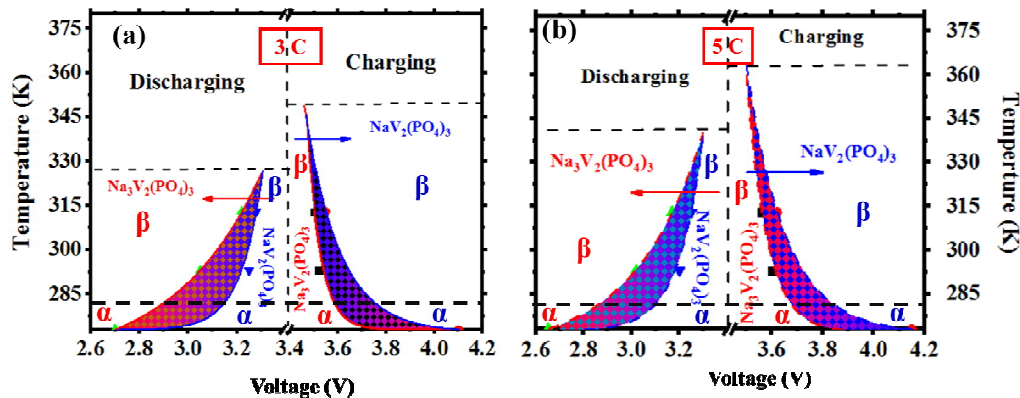


Figure 7. Phase diagrams of $\text{Na}_3\text{V}_2(\text{PO}_4)_3$ during galvanostatic charge and discharge at different current rates of a) 3 C and b) 5 C. In each phase diagram, the horizontal axis represents the voltage range, and temperature is on the vertical axis..

In-situ XRD of $\text{Na}_3\text{V}_2(\text{PO}_4)_3$ at the rates (3 C and 5 C) and the temperatures (273, 293 and 313 K) was performed (Figure S8, Supporting Information) to further investigate the electrochemical reaction mechanism. The result also shows the existence of the asymmetric reaction pathway, which highly consists with the *in-situ* XRD results at different scan rates. To further study the existent condition of the solid solution reaction in such a polyanion-type system, the electrochemical phase diagram of charging and discharging processes is drawn (Figure 7 a and b) based on the acquired data from Figure S8. The occurrence of the solid solution and the formation of the stable charged or discharged phase is regarded as the starting and the ending point. In the *in-situ* data, the slightly peak shift point from the pristine or sodium poor phase is selected, from where the voltage and temperature parameters can be acquired. The formation, development of the solid solution reaction can be deduced from the

1
2
3
4 acquired data, which follows the trend of exponent decay or growth during charging
5
6 or discharging process. It can be observed from the deduced electrochemical phase
7
8 diagram that the reaction is asymmetric and there exists different reaction pathway.
9
10 With the help of the fitted electrochemical phase diagram, the electrochemical
11
12 property of this solid solution and the asymmetric reaction can be easily traced. To
13
14 study the character of the solid solution process, the charge-relax experiment was
15
16 employed at 273 and 293 K where a current equivalent to 10 C is applied for 90 s
17
18 followed by an open-circuit relaxation of 10 min (Figure S9, Supporting Information).
19
20 The electrochemical process presents the solid solution reaction at an elevated current
21
22 density, which is induced by the overpotential. At a low temperature, the occurrence
23
24 the asymmetric reaction becomes more obvious, where temperature is the dominant
25
26 factor rather than current density. This material system shows the similarity with
27
28 $\text{LiFePO}_4/\text{FePO}_4$ system. Compared with our previous work, this material system is
29
30 more complicated and interesting.²³ $\text{LiFePO}_4/\text{FePO}_4$ system shows no phase transition
31
32 induced by temperature during 273 – 293 K. This is due to the not fully occupied site
33
34 position of the sodium in $\text{Na}_3\text{V}_2(\text{PO}_4)_3$ structure.
35
36
37
38
39
40
41
42
43

44 45 **4. CONCLUSIONS**

46
47 The phase transition processes of sodium ion cathode material, $\text{Na}_3\text{V}_2(\text{PO}_4)_3$, are
48
49 investigated at different CV scan rates (0.5, 2 and 5 mV s^{-1}) and temperatures (273 K
50
51 and 293 K) under *operando* conditions, where the asymmetric reaction routes are
52
53 observed. The nonlinear decline trend of the calculated sodium ion diffusion
54
55 coefficients confirm the existence of the asymmetric reaction. *In-situ* XRD result at
56
57
58
59
60

1
2
3 different current densities (3 and 5 C) and temperatures (273, 293 and 333 K) and
4
5
6 further *in-situ* Raman result are in consistence with the assumption. The experiment
7
8
9 result shows that the solid solution reaction can accelerate the phase transformation
10
11 process. The electrochemical phase diagram of $\text{Na}_3\text{V}_2(\text{PO}_4)_3$ is drawn to understand
12
13 the property of the asymmetric reaction in NASICON-type material at different
14
15 temperatures. These observation and analysis can help understanding and developing
16
17 the next generation SIBs with enhanced rate capability and better temperature
18
19 adaptability.
20
21
22

23 24 **ASSOCIATED CONTENT**

25 26 **Supporting Information.**

27
28 The Supporting Information is available free of charge on the ACS Publications
29
30 website.
31
32

33
34 Experiment device, procedures, cycle performances, powder patterns, Raman
35
36 spectrum.
37
38

39 40 **AUTHOR INFORMATION**

41 42 **Corresponding Author**

43
44 *E-mail: ymymiles@whut.edu.cn; mlq518@whut.edu.cn.
45
46

47 48 **Notes**

49
50 The authors declare no competing financial interest.
51
52

53 54 **ACKNOWLEDGMENT**

1
2
3
4 G. Zhang and T. Xiong contributed equally to this work. This work was supported by
5
6 the National Key Research and Development Program of China (2016YFA0202603),
7
8 the Fundamental Research Funds for the Central Universities (WUT 2017-YB-005),
9
10 the National Basic Research Program of China (2013CB934103), the Program of
11
12 Introducing Talents of Discipline to Universities (B17034), the National Natural
13
14 Science Foundation of China (51521001, 51602239), the National Natural Science
15
16 Fund for Distinguished Young Scholars (51425204), and the Fundamental Research
17
18 Funds for the Central Universities (WUT: 2016III001, 2016III003, 2016IVA090).
19
20 Prof. L.Q.M. gratefully acknowledges financial support from the China Scholarship
21
22 Council (No.201606955096) Thanks to Prof. Massimo Nespolo of Université de
23
24 Lorraine for strong support and stimulating discussion.
25
26
27
28
29
30
31

32 REFERENCES

- 33
34 1. Fang, C.; Huang, Y. H.; Zhang, W. X.; Han, J. T.; Deng, Z.; Cao, Y. L.; Yang, H. X., Routes to High Energy
35 Cathodes of Sodium-Ion Batteries. *Adv. Energy Mater.* **2016**, 6, (5), 1501727.
36
37 2. Palacin, M. R.; de Guibert, A., Why do batteries fail? *Science* **2016**, 351, (6273), 1253292.
38
39 3. Kabbour, H.; Coillot, D.; Colmont, M.; Masquelier, C.; Mentre, O., alpha-Na₃M₂(PO₄)₃ (M = Ti, Fe):
40 absolute cationic ordering in NASICON-type phases. *J Am Chem Soc* **2011**, 133, (31), 11900-11903.
41
42 4. Kang, J.; Baek, S.; Mathew, V.; Gim, J.; Song, J.; Park, H.; Chae, E.; Rai, A. K.; Kim, J., High rate
43 performance of a Na₃V₂(PO₄)₃/C cathode prepared by pyro-synthesis for sodium-ion batteries. *J. Mater. Chem.*
44 **2012**, 22, (39), 20857-20860.
45
46 5. Goodenough, J. B.; Hong, H. Y. P.; Kafalas, J. A., Fast Na⁺-ion transport in skeleton structures. *Mater. Res.*
47 *Bull.* **1976**, 11, (2), 203-220.
48
49 6. Hong, H. Y. P., Crystal structures and crystal chemistry in the system Na_{1+x}Zr₂SixP_{3-x}O₁₂. *Mater. Res. Bull.*
50 **1976**, 11, (2), 173-182.
51
52 7. Delmas C, Nadiri A, Soubeyroux J L. The nasicon-type titanium phosphates ATi₂(PO₄)₃ (A= Li, Na) as
53 electrode materials[J]. *Solid State Ionics*, **1988**, 28: 419-423.
54
55 8. Plashnitsa, L. S.; Kobayashi, E.; Noguchi, Y.; Okada, S.; Yamaki, J., Performance of NASICON Symmetric
56 Cell with Ionic Liquid Electrolyte. *J. Electrochem. Soc.* **2010**, 157, (4), A536-A543.
57
58 9. Bianchini, M.; Brisset, N.; Fauth, F.; Weill, F.; Elkaim, E.; Suard, E.; Masquelier, C.; Croguennec, L.,
59 Na₃V₂(PO₄)₂F₃ Revisited: A High-Resolution Diffraction Study. *Chem. Mater.* **2014**, 26, (14), 4238-4247.
60
61 10. Lu, Y. C.; Ma, C.; Alvarado, J.; Dimov, N.; Meng, Y. S.; Okada, S., Improved electrochemical performance
of tin-sulfide anodes for sodium-ion batteries. *J. Mater. Chem. A* **2015**, 3, (33), 16971-16977.

11. An, Q. Y.; Xiong, F. Y.; Wei, Q. L.; Sheng, J. Z.; He, L.; Ma, D. L.; Yao, Y.; Mai, L. Q., Nanoflake-Assembled Hierarchical $\text{Na}_3\text{V}_2(\text{PO}_4)_3/\text{C}$ Microflowers: Superior Li Storage Performance and Insertion/Extraction Mechanism. *Adv. Energy Mater.* **2015**, 5, (10), 1401963-1401973.
12. Chu, Z.; Yue, C., Core-shell structured $\text{Na}_3\text{V}_2(\text{PO}_4)_3/\text{C}$ nanocrystals embedded in multi-walled carbon nanotubes: A high-performance cathode for sodium-ion batteries. *Solid State Ionics* **2016**, 287, 36-41.
13. Lim, S. Y.; Kim, H.; Shakoor, R. A.; Jung, Y.; Choi, J. W., Electrochemical and Thermal Properties of NASICON Structured $\text{Na}_3\text{V}_2(\text{PO}_4)_3$ as a Sodium Rechargeable Battery Cathode: A Combined Experimental and Theoretical Study. *J. Electrochem. Soc.* **2012**, 159, (9), A1393-A1397.
14. Jian, Z.; Han, W.; Lu, X.; Yang, H.; Hu, Y.-S.; Zhou, J.; Zhou, Z.; Li, J.; Chen, W.; Chen, D.; Chen, L., Superior Electrochemical Performance and Storage Mechanism of $\text{Na}_3\text{V}_2(\text{PO}_4)_3$ Cathode for Room-Temperature Sodium-Ion Batteries. *Adv. Energy Mater.* **2013**, 3, (2), 156-160.
15. Ren, W.; Yao, X.; Niu, C.; Zheng, Z.; Zhao, K.; An, Q.; Wei, Q.; Yan, M.; Zhang, L.; Mai, L., Cathodic polarization suppressed sodium-ion full cell with a 3.3V high-voltage. *Nano Energy* **2016**, 28, 216-223.
16. Zhang, G.; Xiong, T.; He, L.; Yan, M.; Zhao, K.; Xu, X., & Mai, L. (2017). Electrochemical *in-situ* X-ray probing in lithium-ion and sodium-ion batteries. *J. of Mater. Sci.*, 52(7), 3697-3718.
17. Chotard, J. N., Rouse, G., David, R., Mentré, O., Courty, M., Masquelier, C. (2015). Discovery of a sodium-ordered form of $\text{Na}_3\text{V}_2(\text{PO}_4)_3$ below ambient temperature. *Chem. Mater.* **2015**, 27, (17), 5982-5987.
18. Pawley, G. S., Unit-cell refinement from powder diffraction scans. *J. Appl. Crystallogr.* **1981**, 14, (6), 357-361.
19. Brünger, A. T., A memory-efficient fast Fourier transformation algorithm for crystallographic refinement on supercomputers. *Acta Crystallogr.* **1989**, 45, (1), 42-50.
20. Trasatti, S.; Petrii, O. A., Real surface area measurements in electrochemistry. *J. Electroanal. Chem.* **2012**, 327, (5), 353-376.
21. Prosini, P. P.; Lisi, M.; Zane, D.; Pasquali, M., Determination of the chemical diffusion coefficient of lithium in LiFePO_4 . *Solid State Ionics* **2002**, 148, (1-2), 45-51.
22. Jian, Z. L.; Zhao, L.; Pan, H. L.; Hu, Y. S.; Li, H.; Chen, W.; Chen, L. Q., Carbon coated $\text{Na}_3\text{V}_2(\text{PO}_4)_3$ as novel electrode material for sodium ion batteries. *Electrochem. Commun.* **2012**, 14, (1), 86-89.
23. Yan M. Y., Zhang G. B., Wei Q. L., Tian X. C., Zhao K. N., An Q. Y., Zhou L., Zhao Y. L., Niu C. J., Ren W. H., He L., Mai L. Q., "In operando observation of temperature-dependent phase evolution in lithium-incorporation olivine cathode", *Nano Energy*, 2016, 22, 406-413.

TOC

